**Authors' Accepted Manuscript** - Composite Structures (2023)
https://doi.org/10.1016/j.compstruct.2023.116789

# Inverse design of programmable Poisson's ratio and in-plane stiffness for generalized four-fold origami

Yao Chen [a,*], Jinbing Liang [a], Pan Shi [a], Jian Feng [a], Pooya Sareh [b], Jiansheng Dai [c]

[a] *Key Laboratory of Concrete and Prestressed Concrete Structures of Ministry of Education, and National Prestress Engineering Research Center, Southeast University, Nanjing 211189, China*
[b] *Creative Design Engineering Lab (Cdel), School of Engineering, University of Liverpool, Liverpool, The Quadrangle, Brownlow Hill, L69 3GH, UK*
[c] *Department of Mechanical and Energy Engineering, Southern University of Science and Technology, Shenzhen 518055, China*

*Keywords:*
Generalized four-fold origami
Inverse design
Negative Poisson's ratio
Variable stiffness
Geometric mechanic
Mechanical metamaterial

A B S T R A C T

Origami-inspired metamaterials and structures exhibit extraordinary properties, including programmable Poisson's ratio and tunable stiffness. Although some research has achieved the programmability of generalized four-fold origami structures, the proposed formulas of Poisson's ratio and stiffness are complex and difficult to be applied for inverse design of origami engineering. Here, the geometric mechanics of a generalized four-fold origami unit with three angles and two lengths controls are studied. The analytical formulas give a great potential of inverse design for in-plane Poisson's ratio and in-plane stiffness. To realize inverse design, the transcendental equation with uninvertible solution is simplified by polynomial fitting method. Moreover, the results are verified by the classical Miura origami results, the existing Origami Simulator tools and the physical polyethylene models. Finally, to make the proposed inverse design applicable to non-zero thickness origami, it is recommended to adopt carbon fiber reinforced polymer shell as the connection of the panel.

## 1. Introduction

Origami structures have unique geometric and mechanical properties uncommonly found in traditional structures, including reconfigurable shape [1–3], negative Poisson's ratio [4–6], and tunable structural stiffness [7]. They have thus been widely developed and applied in varieties of fields, such as biomedicine [8,9], robotics [10–12], aerospace [13–16], structural engineering [17–20] and metamaterials [21–23].

Programmability of origami structures has been extensively studied, including geometry [24–27], Poisson's ratio [28,29], and stiffness [30,31]. Since the structure with negative Poisson's ratio effect has better energy absorption performance than the traditional structure [32], and the stiffness has a great impact on the deformation and impact response of the structure [33], the Poisson ratio and stiffness of origami structures have always been a hot topic. Compared with traditional structures, an origami structure shows foldability. By programming the geometry and mechanics [29], the Poisson's ratio and stiffness of origami structures can be accurately represented by the initial configuration parameters and folding angle. The programmable Poisson's ratio and tunable stiffness of the structures are conducive to inverse design [34], and also have a great role in promoting the programmability of origami metamaterials [35–38]. Thus, the programmability of Poisson's ratio and stiffness and the inverse design of structures are important.

Miura origami structure is one of the most common origami structures, and its mechanics have been studied extensively. Xiang et al. [39] revealed that the arc-Miura was superior to the corresponding monolithic arch in terms of energy absorption. Gao et al. [40] found that rational design of Miura origami cells could reduce peak forces and had better load uniformity while maintaining good specific energy absorption. Pratapa et al. [29] explored the conversion between the Miura origami structure and egg shell structure, as well as the change in Poisson's ratio. Liu et al. [41] proposed a new method to measure the geometric and mechanical parameters of the noisy Miura origami structures. Wei et al. [34] derived analytical formulas for Poisson's ratio and stiffness of Miura origami structure. Inspired by these studies, we intend to study the mechanical properties of a generalized four-fold origami structure, aiming to enrich the engineering applications of origami structures.

To date, several scholars have investigated Poisson's ratio or stiffness of generalized four-fold origami structures. These studies focus on the programmability of Poisson's ratio and stiffness under different

* Corresponding author.
*E-mail address:* chenyao@seu.edu.cn (Y. Chen).

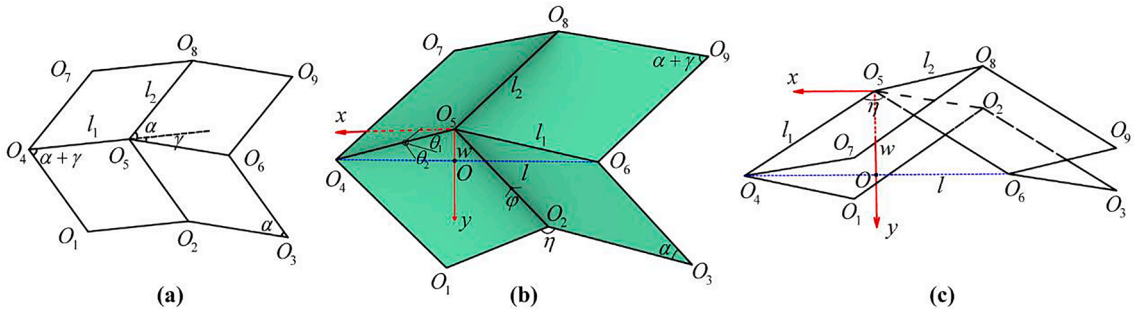


**Fig. 1.** Unit cell of a generalized four-fold origami sheet. (a) Undeformed two-dimensional configuration; (b) Stereogram during folding; (c) Top view during folding.

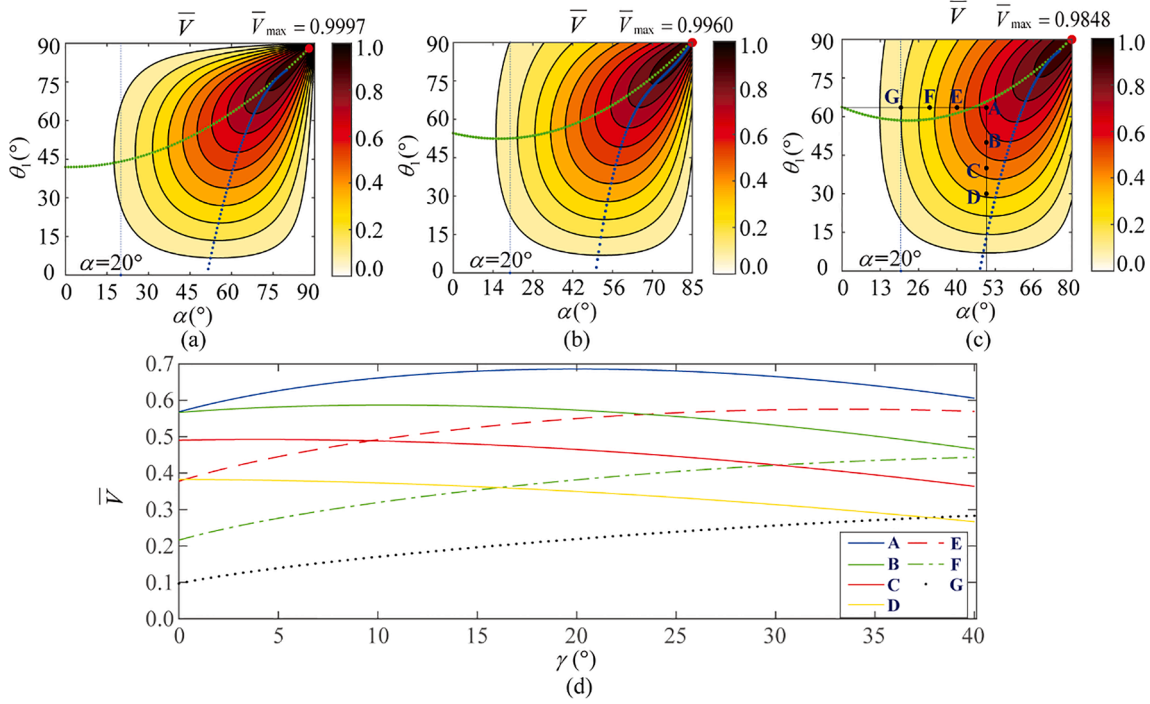


**Fig. 2.** Effective dimensionless apparent volume $\overline{V} = V/(2l_1^2 l_2)$ at (a) $\gamma = 0°$, (b) $\gamma = 5°$, (c) $\gamma = 10°$; (d) $\overline{V}$ of the points with $\alpha = 50°$ and $\theta_1 = 63.54°$ are affected by $\gamma$. Green dotted curve $\theta_{1m}(\alpha)$ indicates the optimal design angle pairs that correspond to the maximum $\overline{V}|\alpha$. Blue dotted curve $\alpha_m(\theta_1)$ indicates the optimal design angle pairs that correspond to the maximum $\overline{V}|\theta_1$. (For interpretation of the references to colour in this figure legend, the reader is referred to the web version of this article.)

configurations and folding angles. Misseroni et al. [6] studied the experimental implementation of tunable Poisson's ratio for generalized four-fold origami metamaterials. Liu et al. [28] proposed a Trimorph origami model, including a generalized Miura origami and a generalized egg shell model. Fang et al. [30] showed that generalized four-fold origami offered new modes of deformation as well as extraordinary kinematic and mechanical properties, and gave the corresponding theoretical formulas. Previous studies on generalized four-fold origami structures have made breakthroughs in stages. However, if this generalized configuration is to be applied as widely as the classical Miura origami structure, exact and robust analytic formulas of its geometric mechanics and quantitative analysis of stiffness with different variables are necessary.

Therefore, we mathematically derive exact expressions to describe the geometric configuration, Poisson's ratio and stiffness of a generalized four-fold origami cell during folding. In addition, the formulas are verified by Origami Simulator, physical polyethylene models and classical Miura origami results. Notably, the polynomial equation is much easier to be reversed than the transcendental equation. Thus, the polynomial fitting method can be used to simplify the formulas, to realize inverse design of generalized four-fold origami structures. The inverse design of geometric mechanics would make this configuration as widely applied in various related fields as the classical Miura origami configuration.

## 2. Basic geometric property

### 2.1. Geometry and kinematics

Fig. 1a shows the unit cell of a generalized four-fold origami sheet in the two-dimensional plane. It consists of four rigid parallelogram plates connected by elastic hinges at the creases, where the panel $O_9O_8O_5O_6$ is equivalent to the panel $O_4O_5O_2O_1$, and the panel $O_4O_5O_8O_7$ is equivalent to the panel $O_3O_2O_5O_6$ [42–45]. In Fig. 1b, the distance between $O_4$ (or $O_6$) and $O_5$ is expressed as $l_1$; the distance between $O_2$ (or $O_8$) and $O_5$ is expressed as $l_2$; the folding angle of the crease $O_5O_2$ (or $O_5O_8$) is defined as $\varphi$; the angle between the crease $O_5O_4$ ($O_2O_1$ or $O_8O_7$) and the crease $O_5O_6$ ($O_2O_3$ or $O_8O_9$) is defined as $\eta$; the height $h$ is the vertical coordinates of $O_7$ ($O_8$ or $O_9$) minus $O_1$ ($O_2$ or $O_3$); $\theta_1$ is the angle between the plane $O_3O_2O_5O_6$ (or $O_4O_5O_8O_7$) and the horizontal plane; $\theta_2$ is the

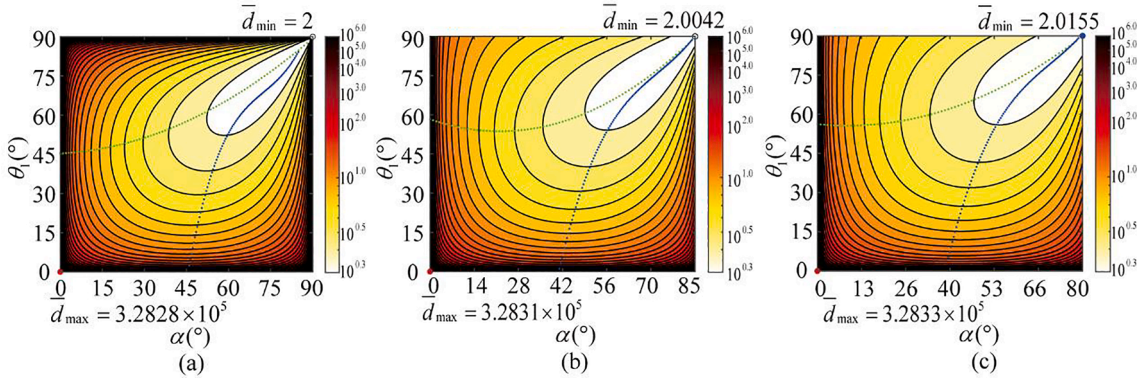


**Fig. 3.** Effective dimensionless relative density $\overline{d} = d/(\rho/l_1)$ at (a) $\gamma = 0°$, (b) $\gamma = 5°$, and (c) $\gamma = 10°$. Green dotted curve $\theta_{1m}(\alpha)$ indicates optimal design angle pairs associated with the maximum $\overline{d}|\alpha$. Blue dotted curve $\alpha_m(\theta_1)$ indicates optimal design angle pairs associated with the maximum $\overline{d}|\theta_1$. (For interpretation of the references to colour in this figure legend, the reader is referred to the web version of this article.)

angle between the plane $O_9O_8O_5O_6$ (or $O_4O_5O_2O_1$) and the horizontal plane; the length $l$ is the distance between point $O_4$ and point $O_6$; and the width $w$ is the distance between point $O_5$ and point $O$. In Fig. 1c, the line $O_4O_6$ is parallel to the $x$-axis; the line $O_5O$ locates on the $y$-axis; and the point $O$ lies on the midpoint of line $O_4O_6$.

The initial configuration of the generalized four-fold origami unit is parameterized by two sides, $l_1$ and $l_2$, and two oblique angles, $\alpha$ and $\gamma$. The folding behavior of the structure can be characterized by two dihedral angles $(\theta_1 + \theta_2) \in [0°,\ 180°]$ and $\varphi \in [0°,\ 180°]$, and the size of the unit cell during folding can be described by the unit length $l$, unit width $w$, and unit height $h$. Since the plate is assumed as rigid, the lengths $l_1$, $l_2$ and $(\alpha+\gamma) \in [0°,\ 90°]$ are constant during folding. Additionally, the length formed by $O_1O_7$ is equal to that formed by $O_3O_9$ (or $O_2O_8$) (that is, plane $O_1O_2O_3$, plane $O_4O_5O_6$, and plane $O_7O_8O_9$ are parallel to the plane $xy$), as shown in Fig. 1b. Thus, it can be obtained that

$$\theta_2 = \frac{180}{\pi}\sin^{-1}\left(\frac{\sin\alpha\sin\theta_1}{\sin(\alpha+\gamma)}\right) \tag{1}$$

As such, we can choose $\theta_1/\theta_2$ (or equivalently $\varphi$) to be the only degree of freedom that completely characterizes a generalized four-fold origami unit. The geometry of the unit cell implies that

$$l = 2l_1\sin\frac{\eta}{2},\ \mathrm{w} = \mathrm{l}_1\cos\frac{\eta}{2},\ \mathrm{h} = 2l_2\xi \tag{2}$$

where $\xi$ is the sine of the angle between the crease $O_5O_2$ (or $O_5O_8$) and the horizontal plane,

$$\xi = \sin\alpha\sin\theta_1 \tag{3}$$

and

$$\eta = \frac{180}{\pi}\cos^{-1}(-\cos\alpha\cos(\alpha+\gamma) + \sin\alpha\sin(\alpha+\gamma)\cos\varphi) \tag{4}$$

where

$$\varphi = \frac{180}{\pi}\cos^{-1}\left(\frac{\sqrt{\left[(\cos\alpha)^2 - (\sin\alpha\cot(\alpha+\gamma))^2\right](\tan\theta_1)^2 + 1} - (\tan\theta_1)^2\cos\alpha\sin\alpha\cot(\alpha+\gamma)}{1 + (\cos\alpha\tan\theta_1)^2}\right) \tag{5}$$

### 2.2. Apparent volume

We explore the variations in the apparent volume of the generalized four-fold origami unit cell during folding. The apparent volume $V$ can be determined by

$$\begin{aligned} V &= lwh = 2l_1^2l_2\xi\sin\eta \\ &= 2l_1^2l_2\sin\alpha\sin\theta_1\sin\left(\cos^{-1}(-\cos\alpha\cos(\alpha+\gamma) + \sin\alpha\sin(\alpha+\gamma)\cos\varphi)\right) \end{aligned} \tag{6}$$

where $\varphi$ is denoted by Eq. (5).

Three different $\gamma$ of 0°, 5°, and 10° are selected to plot the contours of apparent volume $V$. Because $\alpha + \gamma < 90°$, when $\gamma$ increases to 5° or 10°, $\alpha$ cannot exceed 85° or 80°, as shown in Fig. 2a-c. The apparent volume roughly increases with the value of the variable from the bottom left to the top right. Note that at $\alpha = 20°$, the apparent volume of the unit can be changed by changing the value of $\gamma$. As shown in Fig. 2c-d, taking the coordinates of typical configurations A (50°,63.54°), B (50°,50°), C (50°,40°), D (50°,30°), E (40°,63.54°), F (30°,63.54°) and G (20°,63.54°) as examples, the influence of $\gamma$ on apparent volume is analyzed. Under different combinations of ($\alpha$, $\theta_1$), the influence of $\gamma$ is different. When $\alpha < 40°$, the apparent volume increases with the increase of $\gamma$; when $\alpha > 40°$ and $\theta_1 > 60°$, the apparent volume first increases and then decreases with the increase of $\gamma$; when $\alpha > 40°$ and $\theta_1 < 60°$, the apparent volume decreases as $\gamma$ increases. This intuitive relationship facilitates the subsequent determination of initial size of the structure. In particular, it can guide the design of origami structures in engineering applications.

Because the partial derivative of $\eta$ is difficult to inversely solve the theoretical solution, the extreme value for Eq. (7) is obtained by fitting the tangent point of contours in Fig. 2a-c, which is used to estimate the maximum apparent volume and simplify the formulas. On this basis, it is convenient to determine the condition under which the apparent volume takes an extremum at fixed angles $\alpha$ ($\theta_1$) and $\gamma$. This convenience could improve the efficiency of inverse design of origami structures for a specific apparent volume.

$\overline{V}_{\max}|_\alpha^\circ = 0.0062\alpha^2 - 0.0284\alpha + 42.5346$, $\overline{V}_{\max}|\theta_1 = -18.4\theta_1 + 341.3\sqrt{\theta_1} - 1501, at\gamma = 0°$

$\overline{V}_{\max}|_\alpha^\circ = 0.0082\alpha^2 - 0.2811\alpha + 55.2473$, $\overline{V}_{\max}|\theta_1 =$

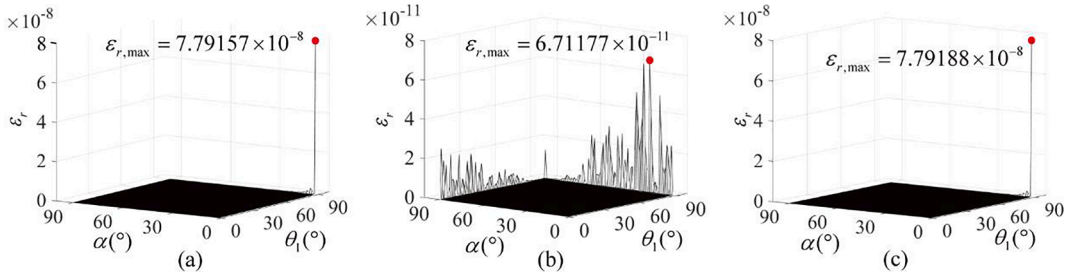


**Fig. 4.** Relative error distributions at $\gamma = 0°$. (a) Poisson's ratio $\nu_{wl}$. (b) Poisson's ratio $\nu_{hl}$. (c) Poisson's ratio $\nu_{hw}$.

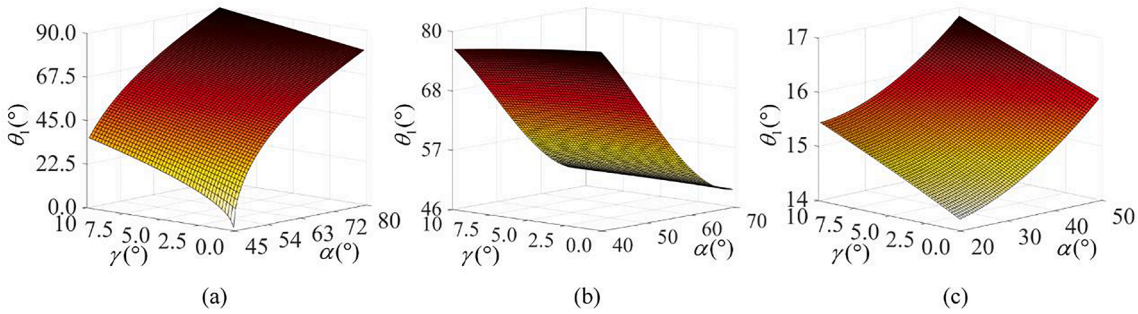


**Fig. 5.** Relationship between the independent variables $\theta_1$, $\alpha$ and $\gamma$ in the case of a special Poisson's ratio (a) when $\nu_{wl} = 1$, (b) when $\nu_{hl} = -1$, (c) when $\nu_{hw} = 1$.

$$0.4376\theta_1^2 - 196\theta_1 + 2276.3\sqrt{\theta_1} - 7397.5 at\ \gamma = 5°$$

$$\overline{V}_{\max}|_{\alpha}^{\circ} = 0.01\alpha^2 - 0.4738\alpha + 64.4364,\ \overline{V}_{\max}|\theta_1 = -19.51\theta_1 + 353.7\sqrt{\theta_1} - 1515\ at\ \gamma = 10° \tag{7}$$

### 2.3. Relative density

We investigate the relative density of the generalized four-fold origami during folding. The relative density $d$ is defined as the ratio between the mass of the structure and the apparent volume occupied by the structure. Assuming that the plate thickness is uniform and the surface density $\rho$ is constant, $d$ can be computed by

$$d = \frac{m}{V} = \frac{2\rho l_1 l_2(\sin(\alpha+\gamma)+\sin\alpha)}{2l_1^2 l_2 \xi \sin\eta} = \frac{\rho(\sin(\alpha+\gamma)+\sin\alpha)}{l_1 \sin\alpha \sin\theta_1 \sin\eta} \tag{8}$$

Fig. 3 shows the contours of the relative density at $\gamma = 0°$, $\gamma = 5°$, and $\gamma = 10°$. The contours can intuitively reflect the variation of $d$ with various angles, i.e., $\theta_1$, $\alpha$, and $\gamma$. When $\gamma$ is a constant, the relative density $d$ decreases with the increase of both $\theta_1$ and $\alpha$. Since the mass is constant during the structure folding, the effect of $\gamma$ on $d$ is opposite to that on $V$ when $\theta_1$ and $\alpha$ are constant.

Similarly, the extreme relative density $\overline{d}$ is determined by fitting the tangent point of contours in Fig. 3, as Eq. (9). It is manifested by the green (blue) dots in Fig. 3. Since the relative density is inversely proportional to the apparent volume, only a small amount of analysis is made on the relative density, and the rest can be further determined by combining the apparent volume analysis.

$$\overline{d}_{\min}|_{\alpha}^{\circ} = 0.0049\alpha^2 + 0.0435\alpha + 45.7948,\quad \overline{d}_{\min}|\theta_1 = 0.002338\theta_1^3 - 0.51\theta_1^2 + 37.98\theta_1 - 895, at\gamma = 0°$$

$$\overline{d}_{\min}|_{\alpha}^{\circ} = 0.0093\alpha^2 - 0.4304\alpha + 59.0502,\quad \overline{d}_{\min}|\theta_1 = 0.001411\theta_1^3 - 0.31\theta_1^2 + 23.7\theta_1 - 551 at\gamma = 5°$$

$$\overline{d}_{\min}|_{\alpha}^{\circ} = 0.0069\alpha^2 - 0.138\alpha + 56.7\overline{d}_{\min}|\theta_1 = 0.00143\theta_1^3 - 0.303\theta_1^2 + 22.46\theta_1 - 499 at\gamma = 10° \tag{9}$$

## 3. Poisson's ratio

### 3.1. Formula derivation and verification

There are three kinds of in-plane Poisson's ratios in the three orthogonal directions. The Poisson's ratios $\nu_{wl}$ involving the width $w$ and length $h$, $\nu_{hl}$ involving the height $h$ and length $l$, and $\nu_{hw}$ involving the height $h$ and width $w$ are determined by Eq. (10), Eq. (11), and Eq. (12), respectively.

$$\nu_{wl} = \nu_{lw}^{-1} = -\frac{dw/w}{dl/l} = \left(\tan\frac{\eta}{2}\right)^2 \tag{10}$$

$$\nu_{hl} = \nu_{lh}^{-1} = -\frac{dh/h}{dl/l} = \frac{-2\tan\frac{\eta}{2}}{\frac{\partial\eta}{\partial\theta_1}\tan\theta_1} \tag{11}$$

$$\nu_{hw} = \nu_{wh}^{-1} = -\frac{dh/h}{dw/w} = \frac{2}{\frac{\partial\eta}{\partial\theta_1}\tan\frac{\eta}{2}\tan\theta_1} \tag{12}$$

where $dl$ represents a slight change in the direction of length $l$, $\eta$ is denoted by Eq. (4), and $\partial\eta/\partial\theta_1$ represents the partial derivative of the ternary function $\eta$ with respect to $\theta_1$. Poisson's ratio of Eq. (10) is defined as the negative ratio of width contraction to length contraction, which describes the coupling of directional deformation in the orthogonal long and wide directions. Poisson's ratio of Eq. (11) and Eq. (12) is similar. It is assumed that the panel of the generalized four-fold origami structure is rigid (i.e., only deformed at the creases). Thus, the main deformation occurs at the creases to achieve significant transformation of the structure, while the influence of tensile deformation of the panel can be ignored [28–30,34].

Since Eq. (11) and Eq. (12) involve the partial derivatives of $\eta$, it is difficult to reverse the analytical solutions. When the precision requirements are not high, the formulas can be simplified by fitting a polynomial (see Appendix A).

When $\gamma = 0°$, the generalized four-fold origami structure is degenerated into a classical Miura origami structure. For the classical Miura origami, the Poisson's ratio in three directions all binary functions of $\alpha$ and $\theta_1$, where $\theta_2 = \theta_1$.

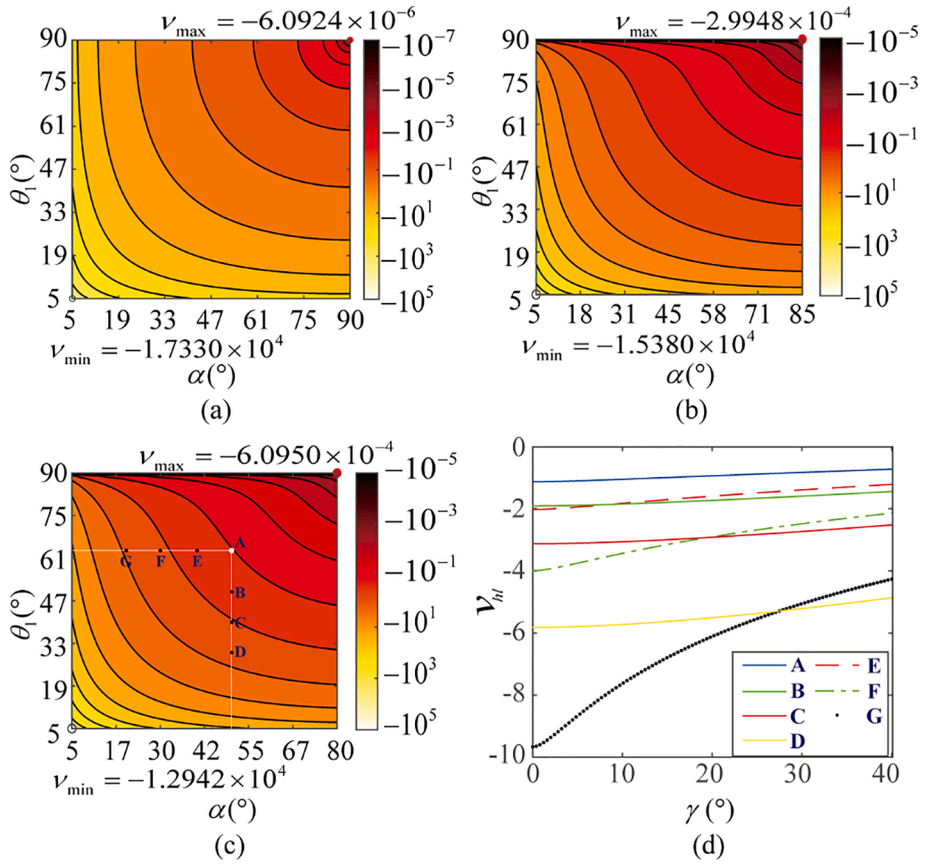


**Fig. 6.** Negative Poisson's ratio $\nu_{hl}$ at (a) $\gamma = 0°$, (b) $\gamma = 5°$, and (c) $\gamma = 10°$. (d) The $\nu_{hl}$ of the points on the line $\alpha = 50°$ and $\theta_1 = 63.54°$ as a function of $\gamma$.

In order to verify the accuracy of the above formulas, we calculate the relative errors of the degenerated Poisson's ratio formulas ($\gamma = 0°$) and the classical Miura origami formulas [34] by

$$\varepsilon_{r\nu_{wl}} = \left|\frac{\nu_{wl}(\theta_1,\alpha) - \nu_{wl}(\theta_1,\alpha,0)}{\nu_{wl}(\theta_1,\alpha)}\right| = \left|\frac{(\cot\alpha)^2(\sec\theta_1)^2 - \left(\tan\frac{\eta}{2}\right)^2}{(\cot\alpha)^2(\sec\theta_1)^2}\right| \leqslant 7.8\times10^{-8} \tag{13}$$

$$\varepsilon_{r\nu_{hl}} = \left|\frac{\nu_{hl}(\theta_1,\alpha) - \nu_{hl}(\theta_1,\alpha,0)}{\nu_{hl}(\theta_1,\alpha)}\right| = \left|\frac{1 - \frac{1}{(\sin\alpha\sin\theta_1)^2} - \frac{-2\tan\frac{\eta}{2}}{\frac{\partial\eta}{\partial\theta_1}\tan\theta_1}}{1 - \frac{1}{(\sin\alpha\sin\theta_1)^2}}\right| \leqslant 6.7\times10^{-11} \tag{14}$$

$$\varepsilon_{r\nu_{hw}} = \left|\frac{\nu_{hw}(\theta_1,\alpha) - \nu_{hw}(\theta_1,\alpha,0)}{\nu_{hw}(\theta_1,\alpha)}\right| = \left|\frac{\frac{1-(\sin\alpha\sin\theta_1)^2}{(\cos\alpha\tan\theta_1)^2} - \frac{2}{\frac{\partial\eta}{\partial\theta_1}\tan\frac{\eta}{2}\tan\theta_1}}{\frac{1-(\sin\alpha\sin\theta_1)^2}{(\cos\alpha\tan\theta_1)^2}}\right| \leqslant 7.8\times10^{-8} \tag{15}$$

The distributions of the relative error size of the Poisson's ratio are shown in Fig. 4a-c. The maximum relative errors are all less than $10^{-7}$ and most of them are less than $10^{-15}$. Because of the truncation error in numerical calculations, the relative error within $10^{-7}$ can be ignored. Therefore, it is verified that the established formulas have high accuracy.

### 3.2. Inverse design of programmable Poisson's ratio

#### 3.2.1. Positive Poisson's ratio

Eq. (10) and Eq. (12) show that both $\nu_{wl}$ and $\nu_{hw}$ are positive. For solid structures, the Poisson's ratio typically varies from $-1$ to 1/2. Interestingly, when the Poisson's ratio is equal to 1, the structure has a reverse amplitude expansion and contraction. As such, we take $\nu_{wl} = 1$ and $\nu_{hw} = 1$ as illustrations (Eq. (16) and Eq. (18)) to explore the relationship between the independent variables $\theta_1$, $\alpha$, and $\gamma$.

$$\nu_{wl} = \nu_{lw}^{-1} = -\frac{dw/w}{dl/l} = \left(\tan\frac{\eta}{2}\right)^2 = 1 \tag{16}$$

which gives the following result (Fig. 5a)

$$\theta_1 = \frac{180}{\pi}\tan^{-1}\left(\frac{\sqrt{-\cos\gamma\cos(2\alpha+\gamma)}}{\cos(\alpha+\gamma)}\right) \tag{17}$$

and

$$\nu_{hw} = \nu_{wh}^{-1} = -\frac{dh/h}{dw/w} = \frac{2}{\frac{\partial\eta}{\partial\theta_1}\tan\frac{\eta}{2}\tan\theta_1} = 1 \tag{18}$$

where the partial derivative of $\eta$ is difficult to find the inverse analytical solution. Thus, the polynomial fitting method is used to approximate it. We take the 80 × 80 × 80 data sets of $\alpha \in [20°,50°]$, $\gamma \in [0°,10°]$ and $\theta_1 \in [10°,40°]$ to fit Eq. (12) to a ternary polynomial, and the average relative error of the polynomial fitting is 2.05%. Then, we set this ternary polynomial as 1, and inversely find the relationship between $\theta_1$ and the other two variables.

The result (Fig. 5c) is given by

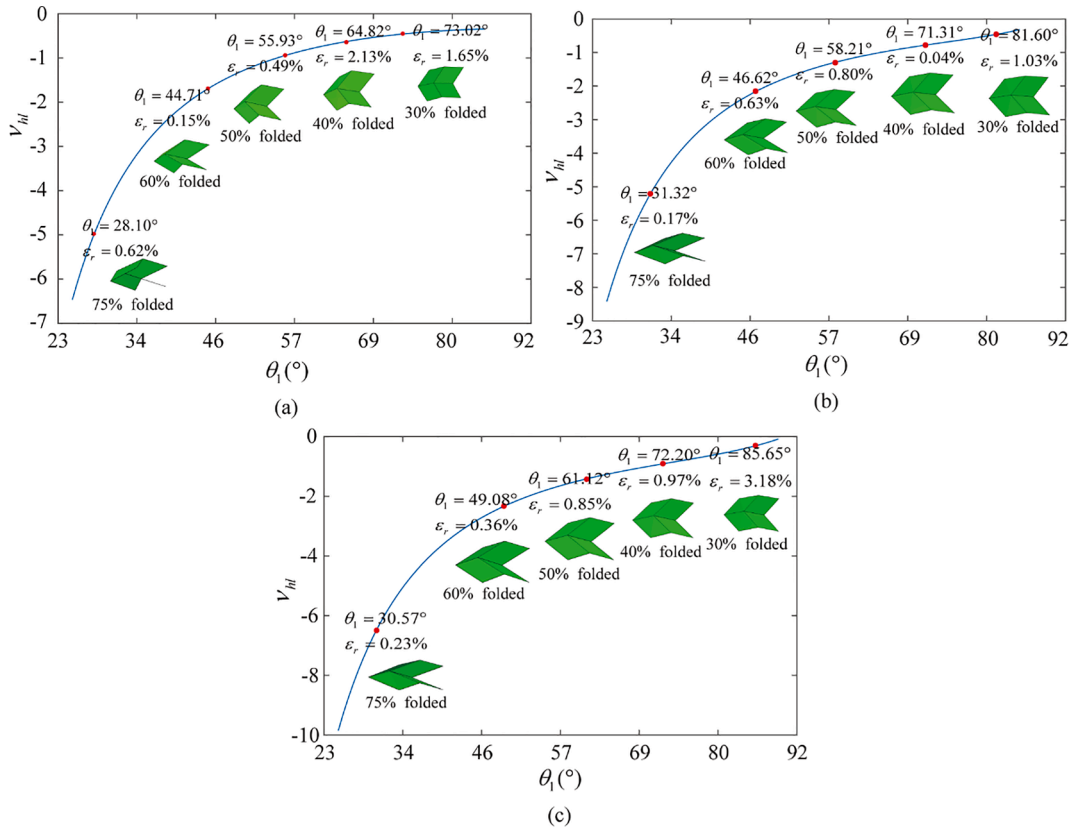


**Fig. 7.** Verification of negative Poisson's ratio based on Origami Simulator. (a) $\alpha = 60°$, $\gamma = 0°$. (b) $\alpha = 50°$, $\gamma = 10°$. (c) $\alpha = 45°$, $\gamma = 15°$.

$$\theta_1 = -0.0212\alpha^3 + 0.0701\alpha^2\gamma + 0.1099\alpha^2 + 0.1165\alpha\gamma^2 - 0.1610\alpha\gamma - 0.0456\alpha + 0.0619\gamma^3 - 0.0131\gamma^2 + 0.2025\gamma + 0.2475 \quad (19)$$

where Eq. (19) is a polynomial numerical solution when $\alpha \in (20°, 50°)$ and $\gamma \in (0°, 10°)$.

### 3.2.2. Negative Poisson's ratio

Eq. (11) shows that the $\nu_{hl}$ is negative. The structure with a negative Poisson's ratio can co-expand or co-contract in two directions. In particular, when the Poisson's ratio is equal to $-1$, the amplitude of co-expansion or co-contraction is the same, which has remarkable research significance [46,47]. The following is to study the relationship between the independent variables $\theta_1$, $\alpha$, and $\gamma$ when $\nu_{hl} = -1$.

$$\nu_{hl} = \nu_{lh}^{-1} = -\frac{dh/h}{dl/l} = \frac{-2\tan\frac{\eta}{2}}{\frac{\partial\eta}{\partial\theta_1}\tan\theta_1} = -1 \quad (20)$$

Similarly, when partial derivatives of $\eta$ which are difficult to solve are involved, polynomial fitting method is used for approximation. We take the 80 × 80 × 80 data sets of $\alpha \in [40°,70°]$, $\gamma \in [0°,10°]$ and $\theta_1 \in [30°,70°]$ to fit Eq. (11) to a ternary polynomial, and the average relative error of polynomial fitting is 2.76%. The result (Fig. 5b) is given by

$$\theta_1 = 3.388\alpha^3 - 0.068\alpha^2\gamma - 8.7456\alpha^2 + 0.7437\alpha\gamma^2 + 0.7106\alpha\gamma + 6.1586\alpha + 1.734\gamma^3 - 1.5928\gamma^2 - 0.6744\gamma + 0.2103 \quad (21)$$

where Eq. (21) is a polynomial numerical solution when $\alpha \in (40°, 70°)$ and $\gamma \in (0°, 10°)$. It should be noted that, most angles are expressed in degrees by default in this study, and the angles $\theta_1$ , $\alpha$, and $\gamma$ in Eq. (19) and Eq. (21) should be expressed in radians. Besides, when the variables located at the line of $\theta_1 = 90°$, $\tan\theta_1$ in Eq. (18) or Eq. (20) will become infinite. In this case, the convergence rate of the polynomial is much less than that of the tangent function. Thereafter, the polynomial fitting method cannot guarantee a certain precision for such a singular case, which should be avoided during origami design. Note that this study mainly focuses on the case of $\theta_1 \leq 90°$; when $\theta_1 = 90°$, the dihedral angle $\theta_1 + \theta_2$ approaches 180°, encompassing all possible folding patterns.

Fig. 5 is the relation diagram of independent variables obtained by inverse design when the Poisson's ratio is 1 or $-1$. Using the same method, we can derive the relationship between three independent variables when Poisson's ratio $\nu_{hl}$ takes any negative value. Similarly, we can derive the relationship between three independent variables when the Poisson's ratio $\nu_{wl}$ or $\nu_{hw}$ is positive. Thereafter, inverse design for origami structures with programmable Poisson's ratio can be achieved.

### 3.2.3. Cloud diagrams of negative Poisson's ratio

We further plot the negative Poisson's ratio affected by three independent variables, as shown in Fig. 6. Since the absolute value of negative Poisson's ratio is rather large when $\theta_1$ or $\alpha$ approaches 0°, both independent variables are considered from 5°. It can be noticed from Fig. 6 that, when $\gamma$ keeps constant, the negative Poisson's ratio $\nu_{hl}$ increases with the increase of $\theta_1$ and $\alpha$. With constant $\theta_1$ and $\alpha$, the increase of $\gamma$ increases $\nu_{hl}$.

As shown in Fig. 6d, typical configurations A, B, C, D, E, F and G mentioned above are taken as examples, to analyze the influence of $\gamma$ on negative Poisson's ratio. The results show that $\nu_{hl}$ increases with the rise of $\gamma$. The increase is larger when $\alpha < 30°$. The programmability of the negative Poisson's ratio is difficult to intuitively design through Eq. (11). By combining it with Fig. 6a-c, we can efficiently find the initial and expected configurations. For example, when a negative Poisson's ratio with a large absolute value is needed, we can deliberately design the initial configuration by combining the cloud images with the graph in Fig. 6d, which can greatly improve computational efficiency.

In engineering applications, to reduce the impact of thickness on inverse design, carbon fiber reinforced polymer shell [48] can be adopted for the connection of the whole structure, rather than thin-walled materials or hinged structures. They can make the actual

**Table 1**
Relative error of Poisson's ratio based on Origami Simulator.

| Configuration | $l$/mm | $h$/mm | $\nu_{os}$ | $\nu_{fit}$ | $\varepsilon_{r\_fit}$ | $\varepsilon_{r\_os}$ |
|---|---|---|---|---|---|---|
| $\alpha = 50°, \gamma = 0°$, 32% folded | 166.61 | 129.97 | −1.0127 | −0.9998 | 0.02% | 1.29% |
| $\alpha = 50°, \gamma = 0°$, 33% folded | 165.61 | 129.18 | | | | |
| $\alpha = 60°, \gamma = 5°$, 53% folded | 120.09 | 129.38 | −0.9768 | −0.9940 | 0.60% | 1.72% |
| $\alpha = 60°, \gamma = 5°$, 54% folded | 118.37 | 127.57 | | | | |
| $\alpha = 60°, \gamma = 10°$, 55% folded | 109.50 | 130.11 | −1.0188 | −1.0045 | 0.45% | 1.43% |
| $\alpha = 60°, \gamma = 10°$, 56% folded | 108.15 | 127.94 | | | | |

**Table 2**
Relative error of Poisson's ratio based on physical polyethylene models.

| Configuration | $l$/mm | $h$/mm | $\nu_{exp}$ | $\nu_{fit}$ | $\varepsilon_{r\_fit}$ | $\varepsilon_{r\_exp}$ |
|---|---|---|---|---|---|---|
| $\alpha = 50°, \gamma = 0°, \theta_1 = 67.39°$ | 167.3 | 130.0 | −0.9841 | −0.9998 | −0.02% | 1.57% |
| $\alpha = 50°, \gamma = 0°, \theta_1 = 66.00°$ | 165.6 | 128.7 | | | | |
| $\alpha = 60°, \gamma = 5°, \theta_1 = 54.67°$ | 120.3 | 130.0 | −1.0059 | −0.9940 | −0.60% | 1.19% |
| $\alpha = 60°, \gamma = 5°, \theta_1 = 53.00°$ | 118.0 | 127.5 | | | | |
| $\alpha = 60°, \gamma = 10°, \theta_1 = 54.04°$ | 110.0 | 128.9 | −1.0240 | −1.0045 | 0.45% | 1.95% |
| $\alpha = 60°, \gamma = 10°, \theta_1 = 53.00°$ | 108.5 | 127.1 | | | | |

negative Poisson's ratio more consistent with the predicted results.

### 3.3. Model verifications

#### 3.3.1. Model verifications by origami simulator

Since negative Poisson's ratio has received more attention among the three Poisson's ratios, only negative Poisson's ratio is verified here. We setup three different initial configurations, including the configuration $\alpha = 60°$, $\gamma = 0°$; $\alpha = 50°$, $\gamma = 10°$; and $\alpha = 45°$, $\gamma = 15°$. Sizes for each panel are $l_1 = l_2 = 100$ mm.

Fig. 7 shows the negative Poisson's ratios calculated by our formulas and the Origami Simulator [49] under the five states of 30%, 40%, 50%, 60%, and 75% folding. In Fig. 7, the blue line is drawn according to Eq. (11) and the red points are drawn by the Origami Simulator.

For the three origami configurations, the maximum relative error between the Origami Simulator and the theoretic formulas are 2.13%, 1.03%, and 3.18%, respectively. Except for the 30% folding state, most of the relative errors are within 1%. The generation of relative errors is because the two adjacent folding states of the Origami Simulator do not change continuously, which are discretization by 1% folding degree [49]. The small errors have indicated the correctness of the proposed formulas.

#### 3.3.2. Verifications for inverse design

Similar to Section 3.3.1, we setup three different initial configurations, including the configuration with $\alpha = 50°$, $\gamma = 0°$; $\alpha = 60°$, $\gamma = 5°$; and $\alpha = 60°$, $\gamma = 10°$. Sizes for each panel are $l_1 = l_2 = 92$ mm. As shown in Table 1, $\theta_1$ calculated by Eq. (21) is used as the input parameter of Origami Simulator, and the corresponding length and width are calculated. Then, the corresponding Poisson's ratio $\nu_{os}$ is calculated by Eq. (22). $\theta_1$ calculated by Eq. (21) is taken as the input of Eq. (11), and the corresponding Poisson's ratio $\nu_{fit}$ is calculated. $\varepsilon_{r\_fit}$ is the relative error caused by $\theta_1$ fitted by Eq. (21), and $\varepsilon_{r\_os}$ is the relative error caused by Origami Simulator.

For the configuration with $\alpha = 50°$, and $\gamma = 0°$, $\theta_1$ calculated by Eq. (21) makes the folding degree in the Origami Simulator between 32% and 33%. The folding of the other two configurations is determined in a similar way. Then, the Poisson's ratio $\nu_{hl}$ is

$$\nu_{hl} = -\frac{(h' - h'')/h'}{(l' - l'')/l'} \tag{22}$$

where $h$' and $h$'' are the corresponding heights of two folded forms of the same configuration, respectively. Similarly, $l$' and $l$'' are the lengths corresponding to two folded configurations. Note that $h' > h''$, $l' > l''$. It can be noticed from Table 1 that, the maximum error of these three models is less than 2%, which further proves the reliability of Eq. (21).

Further, we experimentally study three different origami configurations, to verify the reliability of Eq. (21). To better meet the hypothesis conditions, we choose thin polyethylene membrane to fold the physical polyethylene models [11]. The basic dimensions for each panel are similar to those in Table 1, and the thickness is selected as 0.3 mm. As shown in Table 2, $\theta_1$ calculated by Eq. (21) is used as the input, and the corresponding length and width are calculated. Then, the corresponding Poisson's ratio $\nu_{exp}$ is calculated by Eq. (22). In Table 2, $\varepsilon_{r\_exp}$ is the relative error caused by experiment.

The experimental errors were mainly caused by the bending of the panel, the cutting of physical polyethylene models, and the error of the

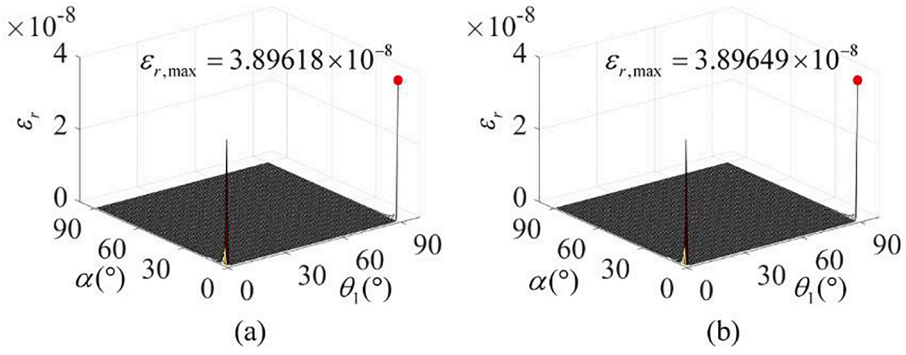


**FIG. 8.** Relative error distributions at $\gamma = 0°$. (a) Tensile stiffness in the $x$ direction. (b) Tensile stiffness in the $z$ direction.

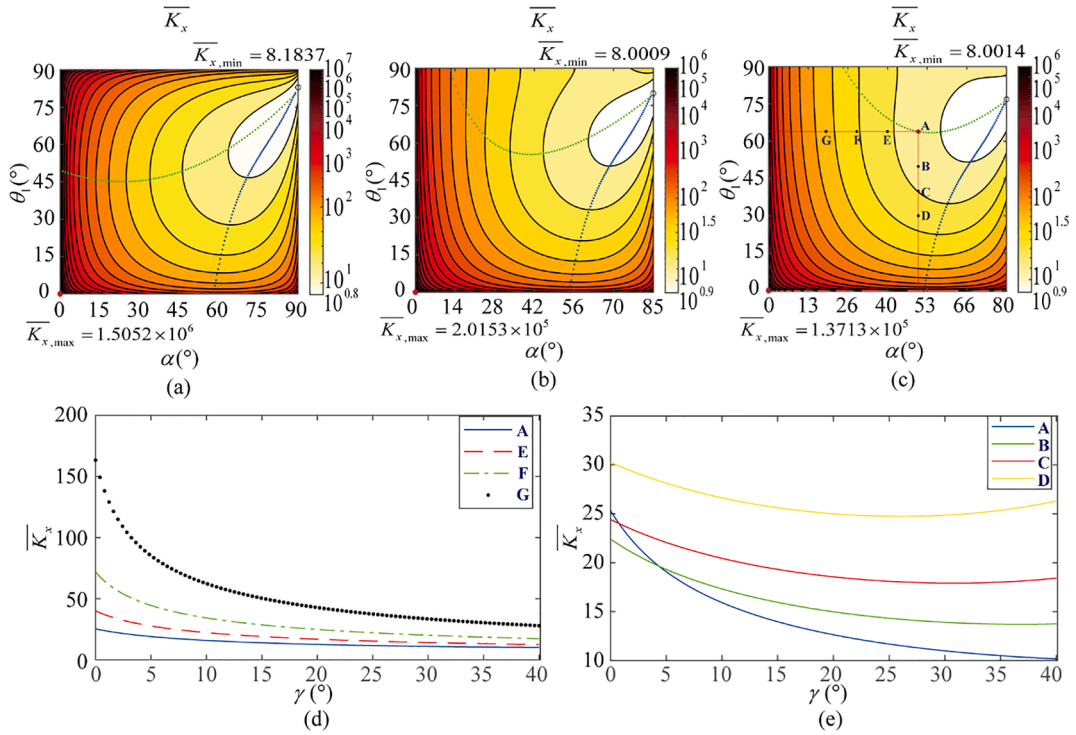


**Fig. 9.** Effective dimensionless stiffness $\overline{K_x} = K_x/k$ at (a) $\gamma = 0°$, (b) $\gamma = 5°$, and (c) $\gamma = 10°$. The green dotted curve $\theta_{1m}(\alpha)$ indicates the optimal design angle pairs that correspond to the maximum $\overline{K_x}|\alpha$. The blue dotted curve $\alpha_m(\theta_1)$ indicates the optimal design angle pairs that correspond to the maximum $\overline{K_x}|\theta_1$. (d) The $\overline{K_x}$ of the points on the line $\theta_1 = 63.54°$ as a function of $\gamma$. (e) The $\overline{K_x}$ of the points on the line $\alpha = 50°$ as a function of $\gamma$. (For interpretation of the references to colour in this figure legend, the reader is referred to the web version of this article.)

scale reading. However, the relative error $\varepsilon_{r\_exp}$ can be controlled within 2%, which indicates that the fitting polynomial is reliable.

## 4. Tensile rigidity

### 4.1. Formula derivation and verification

We further derive exact analytical expressions for in-plane stiffness in the $\times$ and $z$ directions, i.e., $K_x$ and $K_z$. The potential energy of the generalized four-fold origami unit under a uniaxial force $f_x$ in the $\times$ direction is determined by

$$H = U - \int_{\theta_{1,0}}^{\theta_1} f_x \frac{dl}{d\theta_1} d\theta_1 \tag{23}$$

where the unit length $l$ is given by Eq. (2). As the elastic energy $U$ is only at the elastic hinges, the $U$ can be determined by

$$U = kl_1\left(\theta_1 + \theta_2 - \theta_{1,0} - \theta_{2,0}\right)^2 + kl_2(\varphi - \varphi_0)^2 \tag{24}$$

where $\theta_{1,0}$, $\theta_{2,0}$ and $\varphi_0 = \varphi$ ($\theta_{1,0}$, $\alpha$, $\gamma$) are the initial angles at the undeformed state, $k$ is the hinge spring constant. From $\delta H/\delta\theta_{1,0} = 0$, the external force $f_x$ at the equilibrium state can be obtained by

$$f_x = \frac{dU/d\theta_1}{dl/d\theta_1} \tag{25}$$

where $l$ is given by Eq. (2), $U$ is given by Eq. (24). Thus, we obtain the stretching stiffness in the $x$ direction

$$K_x\left(\theta_{1,0},\alpha,\gamma\right) \equiv \frac{df_x}{d\theta_1}|\theta_{1,0} = 2k\frac{\left(1 + \dfrac{\sin\alpha\cos\theta_{1,0}}{\sqrt{\left(\sin(\alpha+\gamma)\right)^2 - \left(\sin\alpha\sin\theta_{1,0}\right)^2}}\right)^2 - \dfrac{\dfrac{l_2}{l_1}\left(\dfrac{\partial\eta}{\partial\theta_{1,0}}\sin\eta\right)^2}{(\cos\eta+\cos\gamma)(\cos\eta+\cos(2\alpha+\gamma))}}{\dfrac{\partial\eta}{\partial\theta_{1,0}}\cos\dfrac{\eta}{2}} \tag{26}$$

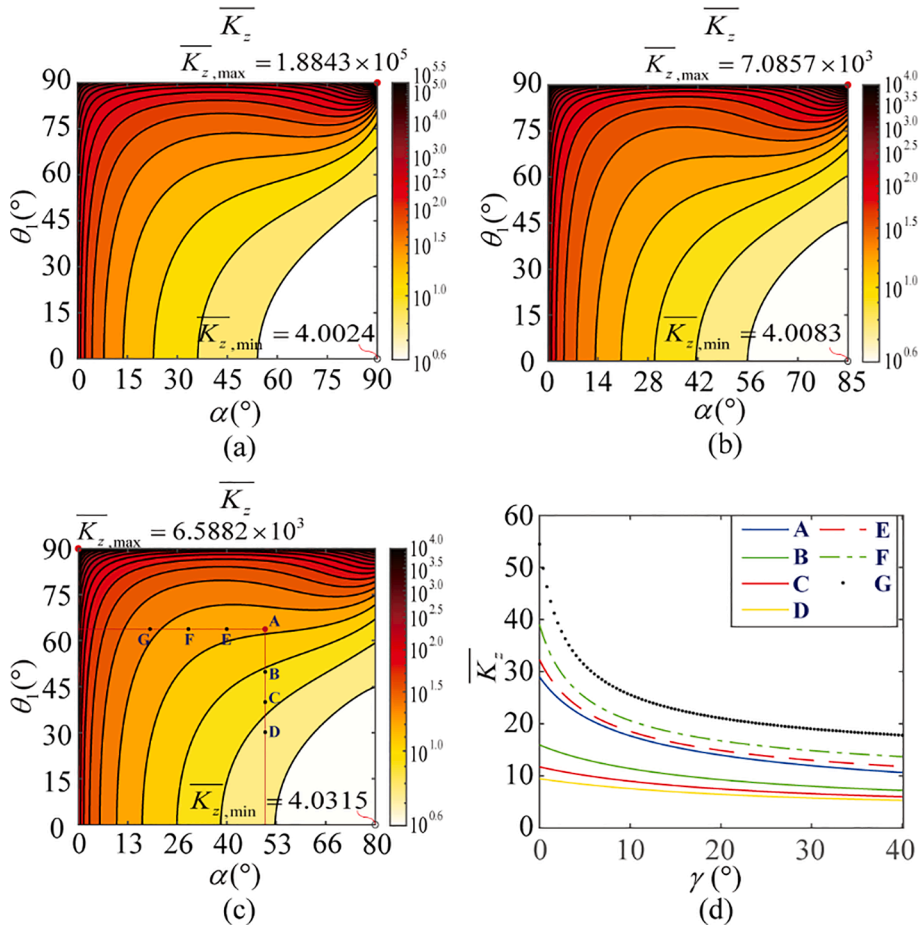


**Fig. 10.** Effective dimensionless stiffness $\overline{K_z} = K_z/k$ at (a) $\gamma = 0°$, (b) $\gamma = 5°$, and (c) $\gamma = 10°$. (d) The $\overline{K_z}$ of the points on the line $\alpha = 50°$ and $\theta_1 = 63.54°$ as a function of $\gamma$.

**Table A1**
The relative errors of every key index of unit cell in 3th-5th degree polynomial fitting.

| $\varepsilon_r$ | $l$ | $w$ | $V$ | $\nu_{wl}$ | $\nu_{hl}$ | $\nu_{hw}$ | $K_x$ | $K_z$ |
|---|---|---|---|---|---|---|---|---|
| $\varepsilon_{r,3}$ | 0.33% | 5.15% | 5.13% | 9.59% | 48.49% | 60.91% | 7.61% | 27.86% |
| $\varepsilon_{r,4}$ | 0.25% | 5.25% | 5.23% | 9.77% | 51.61% | 56.75% | 8.31% | 28.61% |
| $\varepsilon_{r,5}$ | 0.05% | 1.98% | 1.97% | 3.87% | 8.90% | 9.94% | 5.01% | 8.09% |

of which the contours are shown in Fig. 9a-c. In Eq. (26), $\frac{\partial\eta}{\partial\theta_{1,0}}$ is obtained by replacing the variable $\theta_1$ in the derivative $\frac{\partial\eta}{\partial\theta_1}$ with the parameter $\theta_{1,0}$.

Similarly, we can obtain the uniaxial force $f_z$ in the $z$ direction

$$f_z = \frac{dU/d\theta_1}{dh/d\theta_1} \tag{27}$$

and the stretching stiffness in the $z$ direction is

$$K_z(\theta_{1,0},\alpha,\gamma) \equiv \frac{df_z}{d\theta_1}|\theta_{1,0} = k\frac{\frac{l_1}{l_2}\left(1+\frac{\sin\alpha\cos\theta_{1,0}}{\sqrt{(\sin(\alpha+\gamma))^2-(\sin\alpha\sin\theta_{1,0})^2}}\right)^2 - \frac{\left(\frac{\partial\eta}{\partial\theta_{1,0}}\sin\eta\right)^2}{(\cos\eta+\cos\gamma)(\cos\eta+\cos(2\alpha+\gamma))}}{\sin\alpha\cos\theta_{1,0}} \tag{28}$$

of which the contours are shown in Fig. 10.

There are three kinds of in-plane stiffness along the orthogonal directions. Since the stiffness in $x$ and $z$ directions are representative [34], only these two kinds of in-plane stiffness are studied. The stiffness of Eq. (26) is defined as the ratio of the small change in axial force in the $x$ direction to the small change in folding angle $\theta_1$. The stiffness of Eq. (28) is similar. They describe the relationship between axial external force

and axial length variation when the generalized four-fold origami structure is stretched or folded in-plane. Due to the rigid panel assumption of the structure, the large deformation capacity of the structure can be realized by the deformation at the creases. The panel is assumed to be rigid, independent of material properties [30,34].

In the classical Miura origami structure, the stiffness in the $x$ and $z$ directions are both binary functions of $\alpha$ and $\theta_{1,0}$, where $\theta_{1,0} = \theta_{2,0}$. To compare and analyze with the classical Miura origami structure, $l_1 = l_2$ is taken in the degraded stiffness formulas here. In addition, in the process of deriving the formulas, we take the derivation of the variable $\theta_1$. While the classical Miura origami structure directly takes the overall derivation of the variable $(\theta_1 + \theta_2)$. Therefore, in terms of error analysis, the proposed formulas need to be multiplied by a coefficient of 0.5.

Since involving partial derivatives of $\eta$, Eq. (26) and Eq. (28) are extremely complicated. If a certain margin of error is allowed, the formulas can be simplified by fitting a polynomial (see Appendix A). To verify the correctness of the formulas above, we calculate the relative errors of the degraded stiffness formulas ($\gamma = 0°$) and the results of the classical Miura origami structure [34]:

$$\varepsilon_{rK_x} = \left|\frac{K_x(\theta_0,\alpha) - 0.5K_x(\theta_{1,0},\alpha,0)}{K_x(\theta_0,\alpha)}\right| = \left|\frac{4k\dfrac{\left(1-\left(\sin\alpha\sin\theta_{1,0}\right)^2\right)^2+(\cos\alpha)^2}{\cos\alpha(\sin\alpha)^2\sin2\theta_{1,0}\sqrt{1-\left(\sin\alpha\sin\theta_{1,0}\right)^2}} - 0.5\times 2k\dfrac{4-\dfrac{\frac{l_2}{l_1}\left(\frac{\partial\eta}{\partial\theta_{1,0}}\sin\eta\right)^2}{(\cos\eta+1)(\cos\eta+\cos2\alpha)}}{\frac{\partial\eta}{\partial\theta_{1,0}}\cos\frac{\eta}{2}}}{4k\dfrac{\left(1-\left(\sin\alpha\sin\theta_{1,0}\right)^2\right)^2+(\cos\alpha)^2}{\cos\alpha(\sin\alpha)^2\sin2\theta_{1,0}\sqrt{1-\left(\sin\alpha\sin\theta_{1,0}\right)^2}}}\right| \leqslant 3.9\times10^{-8} \tag{29}$$

$$\varepsilon_{rK_z} = \left|\frac{K_z(\theta_0,\alpha) - 0.5K_z(\theta_{1,0},\alpha,0)}{K_z(\theta_0,\alpha)}\right| = \left|\frac{2k\dfrac{\left(1-\left(\sin\alpha\sin\theta_{1,0}\right)^2\right)^2+(\cos\alpha)^2}{\sin\alpha\cos\theta_{1,0}\left(1-\left(\sin\alpha\sin\theta_{1,0}\right)^2\right)^2} - 0.5\times k\dfrac{4\frac{l_1}{l_2}-\dfrac{\left(\frac{\partial\eta}{\partial\theta_{1,0}}\sin\eta\right)^2}{(\cos\eta+1)(\cos\eta+\cos2\alpha)}}{\sin\alpha\cos\theta_{1,0}}}{2k\dfrac{\left(1-\left(\sin\alpha\sin\theta_{1,0}\right)^2\right)^2+(\cos\alpha)^2}{\sin\alpha\cos\theta_{1,0}\left(1-\left(\sin\alpha\sin\theta_{1,0}\right)^2\right)^2}}\right| \leqslant 3.9\times10^{-8} \tag{30}$$

of which the plots are shown in Fig. 8a-b. The maximum relative errors are all less than $10^{-7}$ and most of them are less than $10^{-15}$. It is verified that our established formulas can provide satisfactory accuracy.

### 4.2. Inverse design of tunable stiffness

#### 4.2.1. Cloud diagrams of tensile stiffness in x direction

The change of in-plane stiffness in the $x$ direction with the independent variables is shown in Fig. 10. The stiffness $K_x$ roughly decreases with the value of the variable from the bottom left to the top right. Under different combinations of ($\alpha$, $\theta_1$), the increase of $\gamma$ in a certain range will reduce the stiffness. As shown in Fig. 9d-e, point A (50°, 63.54°) is selected according to the third expression of Eq. (31), and the same coordinates mentioned above are taken as an example to analyze the influence of $\gamma$ on the stiffness $K_x$. The results show that when $\theta_1 > 60°$, $K_x$ decreases with the increase of $\gamma$, and the smaller $\alpha$ is, the more obvious the decrease is; when $\alpha \geq 50°$ and $\theta_1 < 60°$, $K_x$ first decreases and then increases with the increase of $\gamma$, and for smaller $\theta_1$, the ascending segment will be more obvious. In addition, when $\theta_1 < 60°$ but $\alpha < 50°$, there may be no ascending segment, due to the decrease of $\alpha$ can make the ascending segment of $K_x$ disappear.

In particular, with the increase of $\gamma$, the contour twists slowly. Especially, when the folding angle $\theta_1$ is>60° in the range of $\alpha = 25°$-70°, the in-plane stiffness along the $x$ direction decreases significantly as $\gamma$ increases. Consequently, a wide range of origami configurations with relatively weak stiffness can be obtained.

In engineering applications, it is frequently difficult to evaluate the change of stiffness with different angles only from Eq. (26). However, it can be easy to find out the independent variables under the corresponding stiffness more intuitively by using several groups of contour cloud figures.

Since the partial derivative of $\eta$ is difficult to inversely solve the theoretical solution, the extreme value Eq. (31) is obtained by fitting the tangent point of contours in Fig. 9a-c, to estimate the minimum stiffness and simplify the formulas. We can determine the condition that the stiffness takes an extremum under a fixed angle $\alpha$ ($\theta_1$) and $\gamma$. This could improve the efficiency of inverse design of origami configuration for a desired stiffness.

In addition, in order that the structure can still conform to the above inverse design after reciprocating folding, the generalized four-fold origami sheet can be made of copolymer Elvaloy [50]. The Elvaloy is easier to fabricate origami sheet by compression molding compared to traditional materials (such as aluminum, paper and prepreg sheet of carbon fiber), and origami sheet is expected to withstand large and repeated deformation without destroying pattern [51–53].

$$\begin{cases} \overline{K}_{x,\min}|\alpha = 0.0083\alpha^2 - 0.4030\alpha + 50.4829, \text{ at } \gamma = 0^\circ. \\ \overline{K}_{x,\min}|\alpha = 8.4281 \times 10^{-5}\alpha^3 - 0.0266\alpha^2 + 7.8904\alpha - 78.8228\sqrt{\alpha} + 275.7879, \text{ at } \gamma = 5^\circ. \\ \overline{K}_{x,\min}|\alpha = -1.851 \times 10^{-4}\alpha^3 + 0.0554\alpha^2 - 4.4111\alpha + 169.4562, \text{ at } \gamma = 10^\circ. \\ \overline{K}_{x,\min}|\theta_1 = 248.93\theta_1 - 13120\sqrt{\theta_1} + 52013\sqrt[4]{\theta_1} - 58063, \text{ at } \gamma = 0^\circ. \\ \overline{K}_{x,\min}|\theta_1 = 263.53\theta_1 - 13500\sqrt{\theta_1} + 52763\sqrt[4]{\theta_1} - 58063, \text{ at } \gamma = 5^\circ. \\ \overline{K}_{x,\min}|\theta_1 = 296.26\theta_1 - 14319\sqrt{\theta_1} + 54340\sqrt[4]{\theta_1} - 58063, \text{ at } \gamma = 10^\circ. \end{cases} \tag{31}$$

#### 4.2.2. Cloud diagrams of tensile stiffness in z direction

The change of in-plane stiffness in the $z$ direction with three independent variables is shown in Fig. 10. The stiffness $K_z$ decreases with the variable from the top left to the bottom right. As shown in Fig. 10c-d, the increase of $\gamma$ can reduce the stiffness. Under different combinations of ($\theta_1$, $\alpha$), the smaller $\alpha$ is, the more obvious the influence of $\gamma$ increase on the stiffness is. However, the smaller $\theta_1$ is, the less obvious is the effect of increasing $\gamma$ on it. Consequently, it becomes much easier to intuitively find out the value of the three independent variables under the corresponding stiffness, by using several groups of contour cloud figures.

## 5. Conclusion

We have derived the exact expressions for the Poisson's ratio and stiffness of a generalized four-fold origami, which are neatly determined by three independent variables. Two independent variables, $\alpha$ and $\gamma$, determine the initial configuration. The independent variable $\theta_1$ determines the folding state. Based on the exact expressions, we have realized the inverse design of Poisson's ratio and stiffness.

In addition, formulas for Poisson's ratio and stiffness have been verified. Under the condition that the parameter $\gamma = 0^\circ$, the indexes are compared with the corresponding ones of the classical Miura origami structure, and the correctness of each formula is effectively verified. In particular, the negative Poisson's ratio in Eq. (11) is further verified by the results obtained from the origami simulator. The inverse design accuracy of Eq. (21) is verified by numerical and physical polyethylene models. In general, the correctness is verified not only when $\gamma = 0^\circ$, but also when $\gamma \neq 0^\circ$. Additionally, error analysis of $\eta$ is carried out through the analytical and numerical formulas.

Generalized four-fold origami has been investigated in terms of Origami Simulator, experiments and theoretical formulas. The Poisson's ratio and stiffness of generalized four-fold origami are designed using the derived formulas and cloud image analysis method. Further, CFRP shells and copolymer Elvaloy can make the Poisson ratio and stiffness of the structure achieve inverse design for much more specific needs. We have utilized the polynomial approximation method to simplify computation (e.g., the approximation of key index $\eta$ in Appendix A, and the maximum stiffness in the $x$ direction). They can effectively simplify formulas in a certain precision range, which is conducive to application in origami engineering.

*CRediT authorship contribution statement*

**Yao Chen:** Methodology, Resources, Formal analysis, Validation, Investigation, Writing – original draft, Writing – review & editing, Supervision, Project administration, Funding acquisition. **Jinbing Liang:** Conceptualization, Investigation, Data curation, Formal analysis, Validation, Methodology, Software, Writing – original draft, Writing – review & editing. **Pan Shi:** Formal analysis, Software, Writing – review & editing. **Jian Feng:** Supervision, Validation, Writing – review & editing. **Pooya Sareh:** Supervision, Validation, Writing – review & editing. **Jiansheng Dai:** Supervision, Validation, Writing – review & editing.

**Declaration of Competing Interest**

The authors declare that they have no known competing financial interests or personal relationships that could have appeared to influence the work reported in this paper.

**Data availability**

Data will be made available on request.

*Acknowledgments*

This work was supported by the National Natural Science Foundation of China (Grants No. 51978150 and 52050410334), the Southeast University "Zhongying Young Scholars" project, and the Fundamental Research Funds for the Central Universities. The authors are grateful to the editors and anonymous reviewers for their professional comments and valuable suggestions in improving the quality of the paper.

*Data availability*

The data that support plots and related findings of this work are available from the corresponding author upon reasonable request.

## Appendix A. . Simplified design using polynomial fitting

Although the apparent volume, relative density, Poisson's ratio and tensile stiffness of the generalized four-fold origami cell, can be expressed by an accurate ternary function ($\theta_1$, $\alpha$, $\gamma$). The formula has high complexity and is mainly suitable for theoretical research with high-precision.

In this appendix, we discuss a polynomial approximate fitting method for the key indexes that is consist of angle $\eta$ in the cell. All indexes can be roughly estimated by polynomial when the size of each index is roughly predicted or the simplified calculation within a certain error range is allowed. It greatly simplifies the complexity of calculating the partial derivative of the formula. In addition, it is easy to get numerical solutions in differential and integral calculus, which is difficult to achieve with complex formulas. Especially, sometimes there is no analytical solution when solving a variable at a certain value.

The expression of $\eta$ is given by using Eq. (4) and Eq. (5)

$$\eta = \cos^{-1}(-\cos\alpha\cos(\alpha+\gamma) + \sin\alpha\sin(\alpha+\gamma)\cos\varphi) \tag{A1}$$

where

$$\varphi = \cos^{-1}\left(\frac{\sqrt{\left[(\cos\alpha)^2 - (\sin\alpha\cot(\alpha+\gamma))^2\right](\tan\theta_1)^2 + 1} + (\tan\theta_1)^2\cos\alpha\sin\alpha\cot(\alpha+\gamma)}{1 + (\cos\alpha\tan\theta_1)^2}\right) \tag{A2}$$

Using polynomials to approximate $\eta(\theta_1, \alpha, \gamma)$, we can give a series of 80 × 80 × 80 arrays of ($\theta_1$,$\alpha$,$\gamma$). $\alpha$ and $\gamma$ describe the initial configuration characteristics of the cell, and $\theta_1$ describes the degree of folding. When $\theta_1 \in (0°, 70°)$, $\alpha \in (10°, 40°)$ and $\gamma \in (0°, 10°)$ are considered, the maximum relative errors of $\eta(\theta_1,\alpha,\gamma)$ after 3-5th polynomial fitting are 0.81%, 0.35% and 0.12% respectively, which are less than 1%.

### A.1 Cubic polynomial

$$\begin{aligned}\overrightarrow{a_3} = [&-0.0546, -0.2303, -2.9277, 0.7983, -0.5582, -0.3278, 0.2701, 1.9629, -0.2400,\\ &-0.8125, 0.0974, 0.2884, 0.3394, 0.2519, 0.1445, 0.0184, -0.0632, -2.1201, -1.0407, 3.1593]\end{aligned} \tag{A3}$$

$$\overrightarrow{X_3} = \left[\theta_1^3, \alpha^3, \gamma^3, \theta_1^2\alpha, \theta_1^2\gamma, \alpha^2\theta_1, \alpha^2\gamma, \gamma^2\theta_1, \gamma^2\alpha, \theta_1\alpha\gamma, \theta_1^2, \alpha^2, \gamma^2, \theta_1\alpha, \theta_1\gamma, \alpha\gamma, \theta_1, \alpha, \gamma, 1\right] \tag{A4}$$

$$\eta_3 = \overrightarrow{a_3}\cdot\overrightarrow{X_3} \tag{A5}$$

where the angles $\eta_3$, $\theta_1$, $\alpha$and $\gamma$ should be expressed in radians.

(1) Relative error of size and apparent volume

$$\varepsilon_{rl} = \left|\frac{l(\eta) - l(\eta_3)}{l(\eta)}\right| = \left|\frac{2l_1\sin\frac{\eta}{2} - 2l_1\sin\frac{\eta_3}{2}}{2l_1\sin\frac{\eta}{2}}\right| \leqslant 0.33\% \tag{A6}$$

$$\varepsilon_{rw} = \left|\frac{w(\eta) - w(\eta_3)}{w(\eta)}\right| = \left|\frac{l_1\cos\frac{\eta}{2} - l_1\cos\frac{\eta_3}{2}}{l_1\cos\frac{\eta}{2}}\right| \leqslant 5.15\% \tag{A7}$$

$$\varepsilon_{rh} = \left|\frac{h(\eta) - h(\eta_3)}{h(\eta)}\right| = \left|\frac{2l_2\xi - 2l_2\xi}{2l_2\xi}\right| = 0 \tag{A8}$$

$$\varepsilon_{rV} = \left|\frac{V(\eta) - V(\eta_3)}{V(\eta)}\right| = \left|\frac{2l_1^2l_2\xi\sin\eta - 2l_1^2l_2\xi\sin\eta_3}{2l_1^2l_2\xi\sin\eta}\right| \leqslant 5.13\% \tag{A9}$$

Annotation: the comparison interval is $\theta_1 \in (0°, 70°)$, $\alpha \in (10°, 40°)$ and $\gamma \in (0°, 10°)$.

(2) Relative error of Poisson's ratio

$$\varepsilon_{r\nu_{wl}} = \left|\frac{\nu_{wl}(\eta) - \nu_{wl}(\eta_3)}{\nu_{wl}(\eta)}\right| = \left|\frac{\left(\tan\frac{\eta}{2}\right)^2 - \left(\tan\frac{\eta_3}{2}\right)^2}{\left(\tan\frac{\eta}{2}\right)^2}\right| \leqslant 9.59\% \tag{A10}$$

$$\varepsilon_{r\nu_{hl}} = \left|\frac{\nu_{hl}(\eta) - \nu_{hl}(\eta_3)}{\nu_{hl}(\eta)}\right| = \left|\frac{\frac{-2\tan\frac{\eta}{2}}{\frac{\partial\eta}{\partial\theta_1}\tan\theta_1} - \frac{-2\tan\frac{\eta_3}{2}}{\frac{\partial\eta_3}{\partial\theta_1}\tan\theta_1}}{\frac{-2\tan\frac{\eta}{2}}{\frac{\partial\eta}{\partial\theta_1}\tan\theta_1}}\right| \leqslant 48.49\% \tag{A11}$$

$$\varepsilon_{r\nu_{hw}} = \left|\frac{\nu_{hw}(\eta) - \nu_{hw}(\eta_3)}{\nu_{hw}(\eta)}\right| = \left|\frac{\frac{2}{\frac{\partial\eta}{\partial\theta_1}\tan\frac{\eta}{2}\tan\theta_1} - \frac{2}{\frac{\partial\eta_3}{\partial\theta_1}\tan\frac{\eta_3}{2}\tan\theta_1}}{\frac{2}{\frac{\partial\eta}{\partial\theta_1}\tan\frac{\eta}{2}\tan\theta_1}}\right| \leqslant 60.91\% \tag{A12}$$

Annotation: the comparison interval of $\nu_{wl}$ is $\theta_1 \in (0°, 70°)$, $\alpha \in (10°, 40°)$ and $\gamma \in (0°, 10°)$. The comparison interval of $\nu_{hl}$ and $\nu_{hw}$ is $\theta_1 \in (8°, 70°)$, $\alpha \in (10°, 40°)$ and $\gamma \in (0°, 10°)$. Since partial derivatives of $\eta$ are involved in $\nu_{hl}$ and $\nu_{hw}$, the errors in $\nu_{hl}$ and $\nu_{hw}$ exceed tens of thousands when $\theta_1$ approaches 0°, which is trivial and should be excluded.

(3) Relative error of tensile stiffness

The relative error of tensile stiffness in $x$ direction is as follows:

$$\varepsilon_{rK_x} = \left|\frac{K_x(\eta) - K_x(\eta_3)}{K_x(\eta)}\right| \leqslant 7.61\% \tag{A13}$$

where

$$K_x(\eta_3)=2k\frac{\left(1+\frac{\sin\alpha\cos\theta_{1,0}}{\sqrt{(\sin(\alpha+\gamma))^2-\left(\sin\alpha\sin\theta_{1,0}\right)^2}}\right)^2-\frac{\frac{l_2}{l_1}\left(\frac{\partial\eta_3}{\partial\theta_{1,0}}\sin\eta_3\right)^2}{(\cos\eta_3+\cos\gamma)(\cos\eta_3+\cos(2\alpha+\gamma))}}{\frac{\partial\eta_3}{\partial\theta_{1,0}}\cos\frac{\eta_3}{2}} \tag{A14}$$

Note that all the $\eta$ in $K_x(\eta)$ has been replaced with $\eta_3$ to get $K_x(\eta_3)$.

The relative error of tensile stiffness in $z$ direction is expressed by

$$\varepsilon_{rK_z}=\left|\frac{K_z(\eta)-K_z(\eta_3)}{K_z(\eta)}\right|\leqslant 27.86\% \tag{A15}$$

where

$$K_z(\eta_3)=k\frac{\frac{l_1}{l_2}\left(1+\frac{\sin\alpha\cos\theta_{1,0}}{\sqrt{(\sin(\alpha+\gamma))^2-\left(\sin\alpha\sin\theta_{1,0}\right)^2}}\right)^2-\frac{\left(\frac{\partial\eta_3}{\partial\theta_{1,0}}\sin\eta_3\right)^2}{(\cos\eta_3+\cos\gamma)(\cos\eta_3+\cos(2\alpha+\gamma))}}{\sin\alpha\cos\theta_{1,0}} \tag{A16}$$

Note that all the $\eta$ in $K_z(\eta)$ has been replaced with $\eta_3$ to get $K_z(\eta_3)$.

Annotation: the comparison interval of $\varepsilon_r(K_x)$ is $\theta_1\in(15^\circ,70^\circ)$, $\alpha\in(10^\circ,40^\circ)$ and $\gamma\in(0^\circ,10^\circ)$. The comparison interval of $\varepsilon_r(K_z)$ is $\theta_1\in(18^\circ,70^\circ)$, $\alpha\in(10^\circ,40^\circ)$ and $\gamma\in(0^\circ,10^\circ)$. Since partial derivatives of $\eta$ are involved in $\varepsilon_r(K_x)$ and $\varepsilon_r(K_z)$, the errors in $\varepsilon_r(K_x)$ and $\varepsilon_r(K_z)$ exceed tens of thousands when $\theta_1$ approaches $0^\circ$, which is of no significance and should be excluded.

### A.2 Quartic polynomial

The relative error of each index obtained by the quartic polynomial fitting results is similar to that obtained by the cubic polynomial fitting. There is no advantage compared with the cubic polynomial fitting, and thus it will not be repeated here.

### A.3 Quintic polynomial

$$\begin{aligned}\overrightarrow{a_5}=[&-0.0421,-0.1442,-101.8076,-0.1363,-0.0338,-0.0300,0.5474,56.7800,-43.1213,0.8607,\\&2.9709,-0.1724,1.9336,-18.6780,-3.2144,-0.9544,-0.9183,12.6643,0.4285,1.8311,-3.0893,0.1311,\\&0.3094,44.4385,-0.2464,-0.2046,-0.1693,-1.1325,-12.1396,14.8679,-1.1573,1.6215,-0.6151,\\&-0.0815,1.8677,-3.0337,-0.1001,-0.2182,-7.7518,1.4474,-0.2479,0.3865,0.5565,1.7137,-1.2305,\\&-0.6880,-0.0016,0.0522,0.5292,-0.1695,-0.0240,-0.0421,0.0142,-2.0006,-1.0081,3.1410]\end{aligned} \tag{A17}$$

$$\begin{aligned}\overrightarrow{X_5}=[&\theta_1^5,\alpha^5,\gamma^5,\theta_1^4\alpha,\theta_1^4\gamma,\alpha^4\theta_1,\alpha^4\gamma,\gamma^4\theta_1,\gamma^4\alpha,\theta_1^3\alpha^2,\theta_1^3\gamma^2,\alpha^3\theta_1^2,\alpha^3\gamma^2,\gamma^3\theta_1^2,\gamma^3\alpha^2,\theta_1^3\alpha\gamma,\theta_1\alpha^3\gamma,\theta_1\alpha\gamma^3,\\&\theta_1^2\alpha^2\gamma,\theta_1^2\alpha\gamma^2,\theta_1\alpha^2\gamma^2,\theta_1^4,\alpha^4,\gamma^4,\theta_1^3\alpha,\theta_1^3\gamma,\alpha^3\theta_1,\alpha^3\gamma,\gamma^3\theta_1,\gamma^3\alpha,\theta_1^2\alpha^2,\theta_1^2\gamma^2,\alpha^2\gamma^2,\theta_1^2\alpha\gamma,\theta_1\alpha^2\gamma,\theta_1\alpha\gamma^2,\\&\theta_1^3,\alpha^3,\gamma^3,\theta_1^2\alpha,\theta_1^2\gamma,\alpha^2\theta_1,\alpha^2\gamma,\gamma^2\theta_1,\gamma^2\alpha,\theta_1\alpha\gamma,\theta_1^2,\alpha^2,\gamma^2,\theta_1\alpha,\theta_1\gamma,\alpha\gamma,\theta_1,\alpha,\gamma,1]\end{aligned} \tag{A18}$$

$$\eta_5=\overrightarrow{a_5}\cdot\overrightarrow{X_5} \tag{A19}$$

where the angles $\eta_5$, $\theta_1$,$\alpha$, and $\gamma$ should be expressed in radians.

(1) Relative error of size and apparent volume

$$\varepsilon_{rl}=\left|\frac{l(\eta)-l(\eta_5)}{l(\eta)}\right|=\left|\frac{2l_1\sin\frac{\eta}{2}-2l_1\sin\frac{\eta_5}{2}}{2l_1\sin\frac{\eta}{2}}\right|\leqslant 0.05\% \tag{A20}$$

$$\varepsilon_{rw}=\left|\frac{w(\eta)-w(\eta_5)}{w(\eta)}\right|=\left|\frac{l_1\cos\frac{\eta}{2}-l_1\cos\frac{\eta_5}{2}}{l_1\cos\frac{\eta}{2}}\right|\leqslant 1.98\% \tag{A21}$$

$$\varepsilon_{rh}=\left|\frac{h(\eta)-h(\eta_5)}{h(\eta)}\right|=\left|\frac{2l_2\xi-2l_2\xi}{2l_2\xi}\right|=0 \tag{A22}$$

$$\varepsilon_{rV}=\left|\frac{V(\eta)-V(\eta_5)}{V(\eta)}\right|=\left|\frac{2l_1^2l_2\xi\sin\eta-2l_1^2l_2\xi\sin\eta_5}{2l_1^2l_2\xi\sin\eta}\right|\leqslant 1.97\% \tag{A23}$$

Annotation: the comparison interval is $\theta_1\in(0^\circ,70^\circ)$, $\alpha\in(10^\circ,40^\circ)$ and $\gamma\in(0^\circ,10^\circ)$.

(2) Relative error of Poisson's ratio

$$\varepsilon_{r\nu_{wl}}=\left|\frac{\nu_{wl}(\eta)-\nu_{wl}(\eta_5)}{\nu_{wl}(\eta)}\right|=\left|\frac{\left(\tan\frac{\eta}{2}\right)^2-\left(\tan\frac{\eta_5}{2}\right)^2}{\left(\tan\frac{\eta}{2}\right)^2}\right|\leqslant 3.87\% \tag{A24}$$

$$\varepsilon_{r\nu_{hl}} = \left|\frac{\nu_{hl}(\eta) - \nu_{hl}(\eta_5)}{\nu_{hl}(\eta)}\right| = \left|\frac{\frac{-2\tan\frac{\eta}{2}}{\frac{\partial\eta}{\partial\theta_1}\tan\theta_1} - \frac{-2\tan\frac{\eta_5}{2}}{\frac{\partial\eta_5}{\partial\theta_1}\tan\theta_1}}{\frac{-2\tan\frac{\eta}{2}}{\frac{\partial\eta}{\partial\theta_1}\tan\theta_1}}\right| \leqslant 8.90\% \tag{A25}$$

$$\varepsilon_{r\nu_{hw}} = \left|\frac{\nu_{hw}(\eta) - \nu_{hw}(\eta_5)}{\nu_{hw}(\eta)}\right| = \left|\frac{\frac{2}{\frac{\partial\eta}{\partial\theta_1}\tan\frac{\eta}{2}\tan\theta_1} - \frac{2}{\frac{\partial\eta_5}{\partial\theta_1}\tan\frac{\eta_5}{2}\tan\theta_1}}{\frac{2}{\frac{\partial\eta}{\partial\theta_1}\tan\frac{\eta}{2}\tan\theta_1}}\right| \leqslant 9.94\% \tag{A26}$$

Annotation: the comparison interval of $\nu_{wl}$ is $\theta_1 \in (0°,70°)$, $\alpha \in (10°,40°)$ and $\gamma \in (0°,10°)$. The comparison interval of $\nu_{hl}$ and $\nu_{hw}$ is $\theta_1 \in (13°,70°)$, $\alpha \in (10°,40°)$ and $\gamma \in (0°,10°)$. Since partial derivatives of $\eta$ are involved in $\nu_{hl}$ and $\nu_{hw}$, the errors in $\nu_{hl}$ and $\nu_{hw}$ exceed tens of thousands when $\theta_1$ approaches 0°, which is of no significance and should be excluded.

(3) Relative error of tensile stiffness

The relative error of tensile stiffness in $x$ direction is as follows:

$$\varepsilon_{rK_x} = \left|\frac{K_x(\eta) - K_x(\eta_5)}{K_x(\eta)}\right| \leqslant 5.01\% \tag{A27}$$

where

$$K_x(\eta_5) = 2k\frac{\left(1 + \frac{\sin\alpha\cos\theta_{1,0}}{\sqrt{(\sin(\alpha+\gamma))^2 - (\sin\alpha\sin\theta_{1,0})^2}}\right)^2 - \frac{\frac{l_2}{l_1}\left(\frac{\partial\eta_5}{\partial\theta_{1,0}}\sin\eta_5\right)^2}{(\cos\eta_5+\cos\gamma)(\cos\eta_5+\cos(2\alpha+\gamma))}}{\frac{\partial\eta_5}{\partial\theta_{1,0}}\cos\frac{\eta_5}{2}} \tag{A28}$$

Note that all the $\eta$ in $K_x(\eta)$ has been replaced with $\eta_5$ to get $K_x(\eta_5)$.

The relative error of tensile stiffness in $z$ direction is

$$\varepsilon_{rK_z} = \left|\frac{K_z(\eta) - K_z(\eta_5)}{K_z(\eta)}\right| \leqslant 8.09\% \tag{A29}$$

where

$$K_z(\eta_5) = k\frac{\frac{l_1}{l_2}\left(1 + \frac{\sin\alpha\cos\theta_{1,0}}{\sqrt{(\sin(\alpha+\gamma))^2 - (\sin\alpha\sin\theta_{1,0})^2}}\right)^2 - \frac{\left(\frac{\partial\eta_5}{\partial\theta_{1,0}}\sin\eta_5\right)^2}{(\cos\eta_5+\cos\gamma)(\cos\eta_5+\cos(2\alpha+\gamma))}}{\sin\alpha\cos\theta_{1,0}} \tag{A30}$$

Note that all the $\eta$ in $K_z(\eta)$ has been replaced with $\eta_5$ to get $K_z(\eta_5)$.

Annotation: the comparison interval of $\varepsilon_r(K_x)$ is $\theta_1 \in (8°,70°)$, $\alpha \in (10°,40°)$ and $\gamma \in (0°,10°)$. The comparison interval of $\varepsilon_r(K_z)$ is $\theta_1 \in (12°,70°)$, $\alpha \in (10°,40°)$ and $\gamma \in (0°,10°)$. Since partial derivatives of $\eta$ are involved in $\varepsilon_r(K_x)$ and $\varepsilon_r(K_z)$, the errors in $\varepsilon_r(K_x)$ and $\varepsilon_r(K_z)$ exceed a few thousand when $\theta_1$ approaches 0°, which is of no significance and should be excluded.

### A.4 Brief summary

Table A.1 shows the relative errors brought by the 3-5th polynomial fitting to each indicator of the crystal cell. According to the relative errors of the polynomials, the 4th-order polynomial is more complex than the 3rd-order polynomials. However, the accuracy is similar. Therefore, the 4th degree polynomial is not adopted. By comparing the 3rd-order polynomial with the 5th polynomial, it can be found that the accuracy of the 5th-order polynomial is significantly improved. However, in terms of computational complexity, the 3rd-order polynomial is much lower than that of the 5th-order polynomial. Therefore, when the accuracy is high, it is more reasonable to use 5th-order polynomial for simulation. Thereafter, the relative error of all indexes for analytical solution is less than 10%.

Admittedly, since the Poisson's ratio and tensile stiffness indexes involve partial derivative, the relative error between the numerical results and the theoretical formulas will be large when $\theta_1$ close to 0°. $\theta_1$ is considered from a specific angle >0° (e.g., 5°, 8°, or 13°), which could effectively reduce the truncation error.

## References


[1] Wang R, Song Y, Dai JS. Reconfigurability of the origami-inspired integrated 8r kinematotropic metamorphic mechanism and its evolved 6r and 4r mechanisms. Mech. Mach. Theory 2021;161:104245. https://doi.org/10.1016/j.mechmachtheory.2021.104245.

[2] Liu W, Jiang H, Chen Y. 3d programmable metamaterials based on reconfigurable mechanism modules. Adv. Funct. Mater. 2022;32(9):2109865. https://doi.org/10.1002/adfm.202109865.

[3] Chen Y, Xu R, Lu C, Liu K, Feng J, Sareh P. Multi-stability of the hexagonal origami hypar based on group theory and symmetry breaking. Int J Mech Sci 2023;247:108196. https://doi.org/10.1016/j.ijmecsci.2023.108196.

[4] Eidini M, Paulino GH. Unraveling metamaterial properties in zigzag-base folded sheets. Sci. Adv. 2015;1(8). https://doi.org/10.1126/sciadv.1500224. e1500224.

[5] Greaves GN, Greer AL, Lakes RS, Rouxel T. Poisson's ratio and modern materials. Nat. Mater. 2011;10(11):823–37. https://doi.org/10.1038/nmat3134.
[6] Misseroni D, Pratapa PP, Liu K, Paulino GH. Experimental realization of tunable poisson's ratio in deployable origami metamaterials. Extreme Mech. Lett. 2022;53:101685. https://doi.org/10.1016/j.eml.2022.101685.
[7] Zhai Z, Wang Y, Jiang H. Origami-inspired, on-demand deployable and collapsible mechanical metamaterials with tunable stiffness. P Natl Acad Sci Usa 2018;115(9):2032–7. https://doi.org/10.1073/pnas.1720171115.
[8] Knappe GA, Wamhoff E, Read BJ, Irvine DJ, Bathe M. In situ covalent functionalization of DNA origami virus-like particles. ACS Nano 2021;15(9):14316–22. https://doi.org/10.1021/acsnano.1c03158.
[9] Langford T, Mohammed A, Essa K, Elshaer A, Hassanin H. 4d printing of origami structures for minimally invasive surgeries using functional scaffold. Appl Sci-Basel 2021;11(1):332. https://doi.org/10.3390/app11010332.
[10] Ze Q, Wu S, Dai J, Leanza S, Ikeda G, Yang PC, et al. Spinning-enabled wireless amphibious origami millirobot. Nat. Commun. 2022;13(1):3118. https://doi.org/10.1038/s41467-022-30802-w.
[11] Sareh P., Chermprayong P., Emmanuelli M., Nadeem H., Kovac M. Rotorigami: a rotary origami protective system for robotic rotorcraft. Sci Robot 2018;3(22):eaah5228. https://doi.org/10.1126/scirobotics.eaah5228.
[12] Salerno M, Zhang K, Menciassi A, Dai JS. A novel 4-dof origami grasper with an sma-actuation system for minimally invasive surgery. Ieee T Robot 2016;32(3):484–98. https://doi.org/10.1109/TRO.2016.2539373.
[13] Chen Y, Sareh P, Yan J, Fallah AS, Feng J. An integrated geometric-graph-theoretic approach to representing origami structures and their corresponding truss frameworks. J. Mech. Des. 2019;141(9):091402. https://doi.org/10.1115/1.4042791.
[14] Chen Y, Feng J, Sun Q. Lower-order symmetric mechanism modes and bifurcation behavior of deployable bar structures with cyclic symmetry. Int. J. Solids Struct. 2018;139:1–14. https://doi.org/10.1016/j.ijsolstr.2017.05.008.
[15] Wei G, Chen Y, Dai JS. Synthesis, mobility, and multifurcation of deployable polyhedral mechanisms with radially reciprocating motion. J. Mech. Des. 2014;136(9):091003. https://doi.org/10.1115/1.4027638.
[16] Chen Y, Feng J. Folding of a type of deployable origami structures. Int. J. Struct. Stab. Dy. 2012;12(6):1250054. https://doi.org/10.1142/S021945541250054X.
[17] Li J, Chen Y, Feng X, Feng J, Sareh P. Computational modeling and energy absorption behavior of thin-walled tubes with the kresling origami pattern. J. Int. Assoc. Shell Spat. Struct. 2021;62(2):71–81. https://doi.org/10.20898/j.iass.2021.008.
[18] Ciampaglia A, Fiumarella D, Boursier Niutta C, Ciardiello R, Belingardi G. Impact response of an origami-shaped composite crash box: experimental analysis and numerical optimization. Compos. Struct. 2021;256:113093. https://doi.org/10.1016/j.compstruct.2020.113093.
[19] Ye H, Ma J, Zhou X, Wang H, You Z. Energy absorption behaviors of pre-folded composite tubes with the full-diamond origami patterns. Compos. Struct. 2019;221:110904. https://doi.org/10.1016/j.compstruct.2019.110904.
[20] Chen Y, Shi P, Bai Y, Li J, Feng J, Sareh P. Engineered origami crease perforations for optimal mechanical performance and fatigue life. Thin Wall Struct 2023;185:110572. https://doi.org/10.1016/j.tws.2023.110572.
[21] Silverberg JL, Evans AA, McLeod L, Hayward RC, Hull T, Santangelo CD, et al. Using origami design principles to fold reprogrammable mechanical metamaterials. Science 2014;345(6197):647–50. https://doi.org/10.1126/science.1252876.
[22] Schenk M, Guest SD. Geometry of miura-folded metamaterials. P Natl. Acad. Sci. USA 2013;110(9):3276–81. https://doi.org/10.1073/pnas.1217998110.
[23] Surjadi JU, Gao L, Du H, Li X, Xiong X, Fang NX, et al. Mechanical metamaterials and their engineering applications. Adv. Eng. Mater. 2019;21(3):1800864. https://doi.org/10.1002/adem.201800864.
[24] Qiu C, Zhang K, Dai JS. Repelling-screw based force analysis of origami mechanisms. J. Mech. Robot. 2016;8(3):031001. https://doi.org/10.1115/1.4031458.
[25] Zhang L, Zhu S, Li S, Xu G. Analytical form-finding of tensegrities using determinant of force-density matrix. Compos. Struct. 2018;189:87–98. https://doi.org/10.1016/j.compstruct.2018.01.054.
[26] Chen Y, Yan J, Feng J. Geometric and kinematic analyses and novel characteristics of origami-inspired structures. Symmetry 2019;11(9):1011. https://doi.org/10.3390/sym11091101.
[27] Wei GW, Dai JS. Origami-inspired integrated planar-spherical overconstrained mechanisms. J Mech Design 2014;136(5):051003. https://doi.org/10.1115/1.4025821.
[28] Liu K, Pratapa PP, Misseroni D, Tachi T, Paulino GH. Triclinic metamaterials by tristable origami with reprogrammable frustration. Adv. Mater. 2022;2107998. https://doi.org/10.1002/adma.202107998.
[29] Pratapa PP, Liu K, Paulino GH. Geometric mechanics of origami patterns exhibiting poisson's ratio switch by breaking mountain and valley assignment. Phys. Rev. Lett. 2019;122(15):155501. https://doi.org/10.1103/PhysRevLett.122.155501.
[30] Fang H, Li S, Ji H, Wang KW. Uncovering the deformation mechanisms of origami metamaterials by introducing generic degree-four vertices. Phys. Rev. E 2016;94(4–1):043002. https://doi.org/10.1103/PhysRevE.94.043002.
[31] Yang CH, Geng SN, Walker I, Branson DT, Liu JG, Dai JS, et al. Geometric constraint-based modeling and analysis of a novel continuum robot with shape memory alloy initiated variable stiffness. Int J Robot Res 2020;39(14):1620–34. https://doi.org/10.1177/0278364920913929.
[32] Chang Y, Ma P. Energy absorption and poisson's ratio of warp-knitted spacer fabrics under uniaxial tension. Text. Res. J. 2019;89(6):903–13. https://doi.org/10.1177/0040517518758005.
[33] Ma L, Sun H, Lan X. Dynamic response and damage assessment of spherical robot gfrp spherical shell under low velocity impact. Mater Test 2020;62(7):703–15. https://doi.org/10.3139/120.111536.
[34] Wei ZY, Guo ZV, Dudte L, Liang HY, Mahadevan L. Geometric mechanics of periodic pleated origami. Phys. Rev. Lett. 2013;110(21):215501. https://doi.org/10.1103/PhysRevLett.110.215501.
[35] Jiao P. Hierarchical metastructures with programmable stiffness and zero poisson's ratio. APL Mater. 2020;8(5):051109. https://doi.org/10.1063/5.0003655.
[36] Zhang Z, Luce B, Ma C, Xie B, Hu N. Programmable origami-inspired cellular architected building blocks for flow-regulating adaptive weir. Extreme Mech. Lett. 2020;40:100974. https://doi.org/10.1016/j.eml.2020.100974.
[37] Fang H, Chu SA, Xia Y, Wang K. Programmable self-locking origami mechanical metamaterials. Adv. Mater. 2018;30(15):1706311. https://doi.org/10.1002/adma.201706311.
[38] Yasuda H, Yang J. Reentrant origami-based metamaterials with negative poisson's ratio and bistability. Phys. Rev. Lett. 2015;114(18):185502. https://doi.org/10.1103/PhysRevLett.114.185502.
[39] Xiang XM, Lu G, Ruan D, You Z, Zolghadr M. Large deformation of an arc-miura structure under quasi-static load. Compos. Struct. 2017;182:209–22. https://doi.org/10.1016/j.compstruct.2017.09.023.
[40] Gao J, You Z. Origami-inspired miura-ori honeycombs with a self-locking property. Thin Wall Struct 2022;171:108806. https://doi.org/10.1016/j.tws.2021.108806.
[41] Liu Z, Fang H, Wang K, Xu J. A parameter identification method for continuous-time nonlinear systems and its realization on a miura-origami structure. Mech Syst Signal Pr 2018;108:369–86. https://doi.org/10.1016/j.ymssp.2018.02.024.
[42] Chen Y, Yan J, Feng J, Sareh P. Particle swarm optimization-based metaheuristic design generation of non-trivial flat-foldable origami tessellations with degree-4 vertices. J. Mech. Des. 2021;143(1):011703. https://doi.org/10.1115/1.4047437.
[43] Chen Y, Fan L, Bai Y, Feng J, Sareh P. Assigning mountain-valley fold lines of flat-foldable origami patterns based on graph theory and mixed-integer linear programming. Comput. Struct. 2020;239:106328. https://doi.org/10.1016/j.compstruc.2020.106328.
[44] Sareh P. The least symmetric crystallographic derivative of the developable double corrugation surface: computational design using underlying conic and cubic curves. Mater Design 2019;183:108128. https://doi.org/10.1016/j.matdes.2019.108128.
[45] Sareh P, Guest SD. Design of non-isomorphic symmetric descendants of the miura-ori. Smart Mater Struct 2015;24(8):085002. https://doi.org/10.1088/0964-1726/24/8/085002.
[46] Dyskin AV, Pasternak E, Xu Y. Behavior of extreme auxetic and incompressible elastic materials. Phys. Status Solidi B 2017;254(12):1600851. https://doi.org/10.1002/pssb.201600851.
[47] Zheng QS, Chen T. New perspective on poisson's ratios of elastic solids. Acta Mech 2001;150(3–4):191–5. https://doi.org/10.1007/BF01181811.
[48] Zhang Z, Ma W, Wu H, Wu H, Jiang S, Chai G. A rigid thick miura-ori structure driven by bistable carbon fibre-reinforced polymer cylindrical shell. Compos. Sci. Technol. 2018;167:411–20. https://doi.org/10.1016/j.compscitech.2018.08.033.
[49] Ghassaei A., Demaine ED., Gershenfeld N. Fast, interactive origami simulation using gpu computation. in Origami7: Proceedings of the 7th International Meeting on Origami in Science, Mathematics and Education (OSME 2018), Oxford, England2018. p. 1151-66.
[50] Liu S, Lu G, Chen Y, Leong YW. Deformation of the miura-ori patterned sheet. Int. J. Mech. Sci. 2015;99:130–42. https://doi.org/10.1016/j.ijmecsci.2015.05.009.
[51] Chen Y, Lu C, Yan J, Feng J, Sareh P. Intelligent computational design of scalene-faceted flat-foldable tessellations. J. Comput. Des. Eng. 2022;9:1765–74. https://doi.org/10.1093/jcde/qwac082.
[52] Zhang P, Fan W, Chen Y, Feng J, Sareh P. Structural symmetry recognition in planar structures using convolutional neural networks. Eng. Struct. 2022;260:114227. https://doi.org/10.1016/j.engstruct.2022.114227.
[53] Jalali E, Soltanizadeh H, Chen Y, Xie YM, Sareh P. Selective hinge removal strategy for architecting hierarchical auxetic metamaterials. Nat. Commun. Mater. 2022;3:97. https://doi.org/10.1038/s43246-022-00322-7.